RSC Advances

PAPER

View Article Online
View Journal | View Issue

Check for updates

Cite this: *RSC Adv.*, 2019, **9**, 37556

Ultrafine MoO_2 nanoparticles encapsulated in a hierarchically porous carbon nanofiber film as a high-performance binder-free anode in lithium ion batteries

Xin Chen,[a] Guojun Gao,[a] Zhipeng Wu,[a] Jun Xiang,*[a] Xiaoqiang Li,[a] Guangguang Guan[a] and Kaiyin Zhang*[b]

Received 11th September 2019
Accepted 11th November 2019

DOI: 10.1039/c9ra07307h

rsc.li/rsc-advances

Flexible free-standing hierarchically porous carbon nanofibers embedded with ultrafine (~3.5 nm) MoO_2 nanoparticles (denoted as MoO_2@HPCNFs) have been synthesized by electrospinning and subsequent heat treatment. When evaluated as a binder-free anode in Li-ion batteries, the as-obtained MoO_2@HPCNFs film exhibits excellent capacity retention with high reversible capacity (≥1055 mA h g^{-1} at 100 mA g^{-1}) and good rate capability (425 mA h g^{-1} at 2000 mA g^{-1}), which is much superior to most of the previously reported MoO_2-based materials. The synergistic effect of uniformly dispersed ultrasmall MoO_2 nanoparticles and a three-dimensionally hierarchical porous conductive network constructed by HPCNFs effectively improve the utilization rate of active materials, enhance the transport of both electrons and Li^+ ions, facilitate the electrolyte penetration, and promote the Li^+ storage kinetics and stability, thus leading to a greatly enhanced electrochemical performance.

Open Access Article. Published on 18 November 2019. Downloaded on 12/9/2025 12:40:41 AM.
This article is licensed under a Creative Commons Attribution-NonCommercial 3.0 Unported Licence.

1. Introduction

Rechargeable lithium ion batteries (LIBs) have attracted tremendous attention due to their huge successes in electrochemical energy storage systems.[1–4] Notwithstanding the remarkable progress achieved so far, it is still a great challenge to develop new high-performance electrode materials with high energy density, excellent cycling stability and rate capability to meet the ever-expanding demands for advanced energy storage and conversion devices.[5] Until now, a large number of transition metal oxides have been exploited as promising anode materials for LIBs.[6] Among various metal oxide-based electrode materials, molybdenum dioxide (MoO_2) has been widely studied because of its rich chemical and structural versatility, and high theoretical specific capacity (838 mA h g^{-1}).[7] However, bare MoO_2 is not an ideal Li-storage host due to its intrinsically slow electrochemical reaction kinetics, low conductivity, and drastic volume change during cycling, leading to poor rate capability and severe capacity fading.[8]

To overcome these drawbacks and improve the electrochemical properties, nanosized MoO_2 combined with carbon materials owning good conductivity and structural stability has been demonstrated to be an effective strategy.[9–11] Among diverse carbon materials for LIB anodes, one-dimensional carbon nanofibers (CNFs) and their derivatives have gained special attention because they can be built into a flexible porous three-dimensionally (3D) conductive network for the rapid transport of both electrons and ions, significantly enhancing the electrochemical reaction kinetics and promoting the energy density and cycling stability.[12,13] Moreover, some research has indicated that the introduction of various porous structures into CNFs can further improve both the specific capacity and the rate performance of CNFs-based electrodes.[14,15] The incorporated pores can probably provide more electrode–electrolyte interface and markedly reduce electronic/ionic diffusion distance, thus further strengthening charge transport capability. In recent years, ultrasmall transition metal oxide nanoparticles loaded porous CNFs (PCNFs) have emerged as novel anode materials for LIBs. For instance, TiO_2@PCNFs,[16] MOUNPs@HPCNFs (M = Zn, Mn, and Co),[17] γ-Fe_2O_3/PCNFs,[18] and MoO_3/PCNFs[19] have been reported to exhibit excellent electrochemical properties. However, as far as we know, there has been no report as yet on the preparation and electrochemical performance of flexible self-supported PCNFs containing ultrasmall MoO_2 nanoparticles. Therefore, it is of great interest to design and synthesize such nanostructure as binder-free anodes in LIBs.

Herein, we have proposed a novel binder-free LIB anode based on ultrafine MoO_2 nanoparticles uniformly encapsulated in hierarchically porous carbon nanofibers (denoted as MoO_2@HPCNFs) prepared *via* a facile electrospinning approach using polymethylacrylate (PMMA) as a pore-forming

[a]*School of Science, Jiangsu University of Science and Technology, Zhenjiang 212003, China. E-mail: jxiang@just.edu.cn*

[b]*School of Physics and Electronic Engineering, Fuyang Normal University, Fuyang 236037, China. E-mail: kyzhang@fync.edu.cn*

This journal is © The Royal Society of Chemistry 2019

Open Access Article. Published on 18 November 2019. Downloaded on 12/9/2025 12:40:41 AM.
This article is licensed under a Creative Commons Attribution-NonCommercial 3.0 Unported Licence.

agent, followed by a controlled reduction–carbonization process The MoO_2@HPCNFs electrode exhibits high lithium storage capacity and rate capability, showing a great application prospect in high-performance LIBs.

2. Experimental

2.1. Preparation of MoO_2@HPCNFs

The MoO_2@HPCNFs were prepared *via* co-electrospinning of polyacrylonitrile (PAN)/polymethylacrylate (PMMA)/Mo precursor combined with a controlled reduction–carbonization process, which was similar to our previous report.[20] PMMA was used here as a pore generator that can be removed from the PAN-derived carbon nanofiber matrix under high temperature. 1.76 g of PAN (M_w = 150 k, Aldrich) and 0.44 g of PMMA (M_w = 150 k, Aladdin) were dissolved first in 16.8 g of *N*,*N*-dimethylformamide (DMF) at 60 °C for 4 h under magnetic stirring. Then, 1 g of $MoCl_5$ was added into the mixture solution and further stirred approximately 12 h at room temperature to obtain a homogeneous solution for electrospinning. The precursor solution was transferred into a 20 mL plastic syringe and was electrospun by using a TL-01 electrospinning apparatus under the applied voltage of 18 kV, solution feeding rate of 0.4 mL h^{-1} and collector distance of 18 cm. The as-spun fibers were collected by an aluminum foil enwrapped roller with a rotate speed of about 300 rpm. The formed fiber film was subsequently stabilized at 220 °C for 4 h under air atmosphere and finally carbonized at 600 °C for 5 h in a flowing N_2/H_2 (5 : 1, v/v) mixed atmosphere to yield the resulting product.

2.2. Characterization

The phase structure of as-prepared MoO_2@HPCNFs was analyzed by X-ray diffraction (XRD, Shimadzu, XRD-6000). The surface morphology and microstructure of the sample were observed using field-emission scanning electron microscope (FESEM, Zeiss, Merlin Compact) and high-resolution transmission electron microscope (HRTEM, JEOL, JEM-2001F). Raman spectrum was collected at ambient temperature on a Raman spectrometer (Renishaw, inVia Reflex) using 532 nm excitation wavelength. Thermogravimetric analysis (TGA) was conducted on a TGA apparatus (Shimadzu, DTG-60H) in air. X-ray photoelectron spectroscopy (XPS) measurement was performed on a Thermo Fisher Scientific ESCALAB 250Xi XPS System with a monochromatic Al Kα X-ray source. Nitrogen adsorption/desorption isotherms (BET technique) at 77 K were recorded on a Micromeritics ASAP 2020 analyzer to characterize the pore structure of the product.

2.3. Electrochemical measurements

The obtained MoO_2@HPCNFs film was punched into circular discs and directly utilized as binder-free anodes for electrochemical measurements using CR2025 coin-type cells assembled in a highly pure argon-filled glovebox. Lithium metal foil was employed as the counter electrode, Celgard 2400 microporous polypropylene membrane as the separator, and 1 M $LiPF_6$ in a mixture of ethylene carbonate (EC), ethyl methyl carbonate (EMC) and dimethylcarbonate (DMC) (1 : 1 : 1, v/v/v) as the electrolyte. The galvanostatic charge/discharge tests were carried out on a Land CT2001A battery testing system within the voltage range of 0.01–3.0 V *vs.* Li^+/Li at different current densities. Cyclic voltammetry (CV) was measured by using a BioLogic SP-300 electrochemical workstation between 0.01–3.0 V *vs.* Li^+/Li at a scan rate of 0.1 mV S^{-1}. The mass of self-standing MoO_2@HPCNFs film electrode is around 3 mg, and all the specific capacities are calculated based on the total mass of MoO_2@HPCNFs film in this paper.

3. Results and discussion

Fig. 1a shows the XRD pattern of MoO_2@HPCNFs. All the distinct diffraction peaks can be indexed to the monoclinic structure of MoO_2 (JCPDS no. 73-1249), and no other distinguishable crystalline peaks belonging to molybdenum carbide/nitride are detected in the pattern, suggesting the high purity of the sample. In addition, a broad peak at low angle rang in the baseline can be clearly observed, demonstrating that the HPCNFs matrix is mainly amorphous. The structural information of carbon is further investigated using Raman spectra as presented in Fig. 1b. The as-prepared sample displays two wide peaks located at about 1324 and 1586 cm^{-1}, known as the D-band and G-band, corresponding to the disordered carbon and graphite carbon, respectively.[21] This result indicates that the sample is partially graphitized during the carbonization process. A large number of defects and vacancies in amorphous carbon can offer more diffusion channels and intercalation sites for Li^+ storage, and meanwhile the appearance of graphite carbon can endow the whole film electrode with better conductivity, both of which would contribute to the overall capacity.[17,22] The mass fraction of MoO_2 in the MoO_2@HPCNFs is determined by TGA (Fig. 1c). A small weight loss of 6.5 wt% before 170 °C in the TG curve may be attributed to the evaporation of the absorbed water. The large weight loss of 72.7 wt% from 290 to 510 °C is caused by the combustion of carbon. Consequently, the content of MoO_2 in the MoO_2@HPCNFs is estimated to be about 22.4 wt%.

XPS technique was utilized to analyze the composition and valence states of MoO_2@HPCNFs. As shown in Fig. 1d, the survey spectrum reveals that the composite is composed of O, C and Mo elements. The high-resolution Mo 3d spectrum (Fig. 1e) can be fitted to two doublets.[23] One doublet with low energy and high intensity centered at 235.9 and 232.8 eV are ascribed to Mo(IV) $3d_{3/2}$ and Mo(IV) $3d_{5/2}$, respectively, further confirming the formation of MoO_2. The other doublet with high energy and low intensity at 236.5 and 233.4 eV arise from Mo(VI) $3d_{3/2}$ and Mo(VI) $3d_{5/2}$ of MoO_3, probably due to the slight surface oxidation of metastable MoO_2 in air. Nevertheless, the XRD spectrum in Fig. 1a do not display any peaks coming from MoO_3, which may be because of the low content of MoO_3 or its amorphous nature in the product.

Fig. 2a presents the SEM image of MoO_2@HPCNFs. The HPCNFs have smooth surface and continuous 1D structure with a mean diameter of 420 ± 50 nm and length of up to several hundred microns, which are randomly oriented and interlinked

Open Access Article. Published on 18 November 2019. Downloaded on 12/9/2025 12:40:41 AM.
This article is licensed under a Creative Commons Attribution-NonCommercial 3.0 Unported Licence.

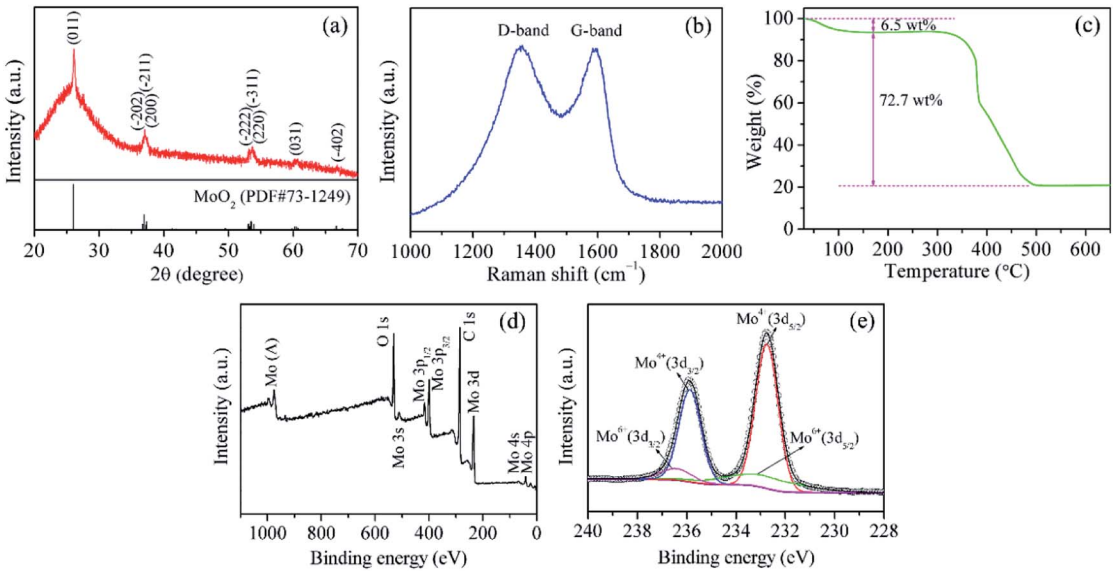

Fig. 1 (a) XRD pattern, (b) Raman spectrum, (c) TG curve, (d) XPS survey spectrum, and (e) high-resolution Mo 3d spectrum of MoO_2@HPCNFs.

into a porous 3D conductive network. Such architecture can endow the electrode with improved cell reaction kinetics and structural integrity for lithium insertion/extraction.[24] Furthermore, the cross-section SEM image (Fig. 2b) reveals that there are numerous mesopores and macropores inside the HPCNFs. The TEM image (Fig. 2d) further verifies this result, and we can also see that the partial MoO_2@HPCNFs have a hollow structure possibly due to the connection of some channel-like macropores. The nitrogen adsorption–desorption isotherm of MoO_2@HPCNFs (Fig. 2c) shows a typical type-IV behavior with an obvious hysteresis loop corresponding to the mesoporous structure, and meanwhile the isotherm displays a steep uptake at high relative pressures ($P/P_0 > 0.8$), also indicating the existence of macroporous structure in the material,[25] which are well accord with the FESEM and TEM observations. By using the BET method, the total pore volume and specific surface area of MoO_2@HPCNFs are approximately 0.13 $cm^3\ g^{-1}$ and 56.6 $m^2\ g^{-1}$, respectively. The abundant mesopores and macropores throughout the HPCNFs not only enable the electrode more fully accessible to the electrolyte and take full advantage of the dispersed high-capacity MoO_2 nanoparticles, but also effectively tolerate the mechanical stress caused by volume change and

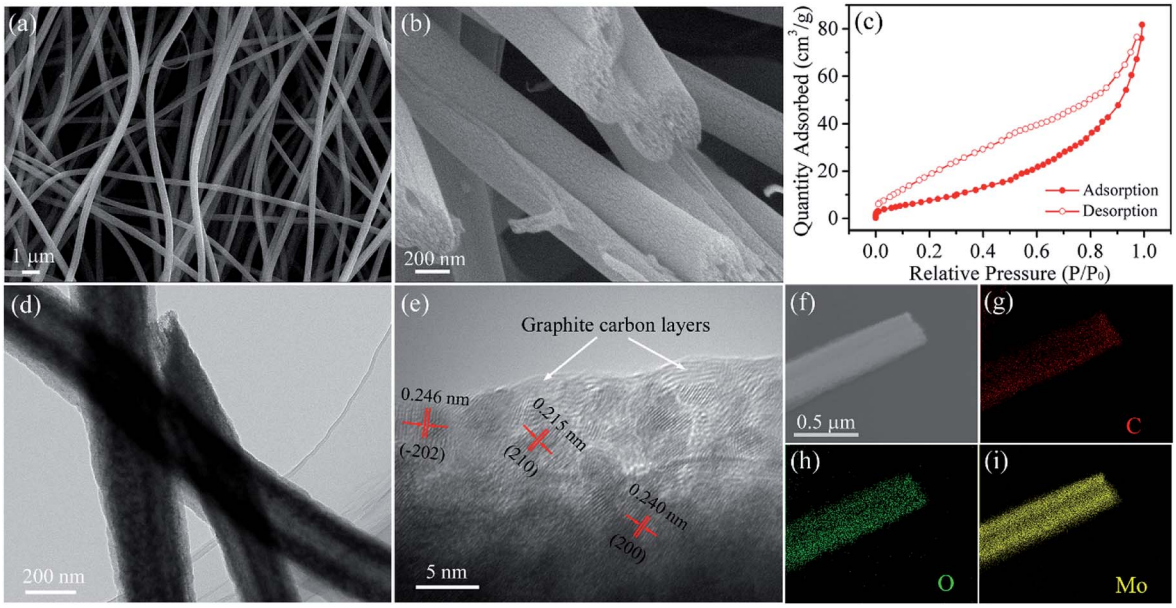

Fig. 2 (a) Surface and (b) cross-sectional SEM images, (c) nitrogen adsorption–desorption isotherm, (d) TEM, (e) HRTEM, (f) STEM and (g–i) corresponding elemental mapping images of MoO_2@HPCNFs.

This journal is © The Royal Society of Chemistry 2019

Open Access Article. Published on 18 November 2019. Downloaded on 12/9/2025 12:40:41 AM.
This article is licensed under a Creative Commons Attribution-NonCommercial 3.0 Unported Licence.

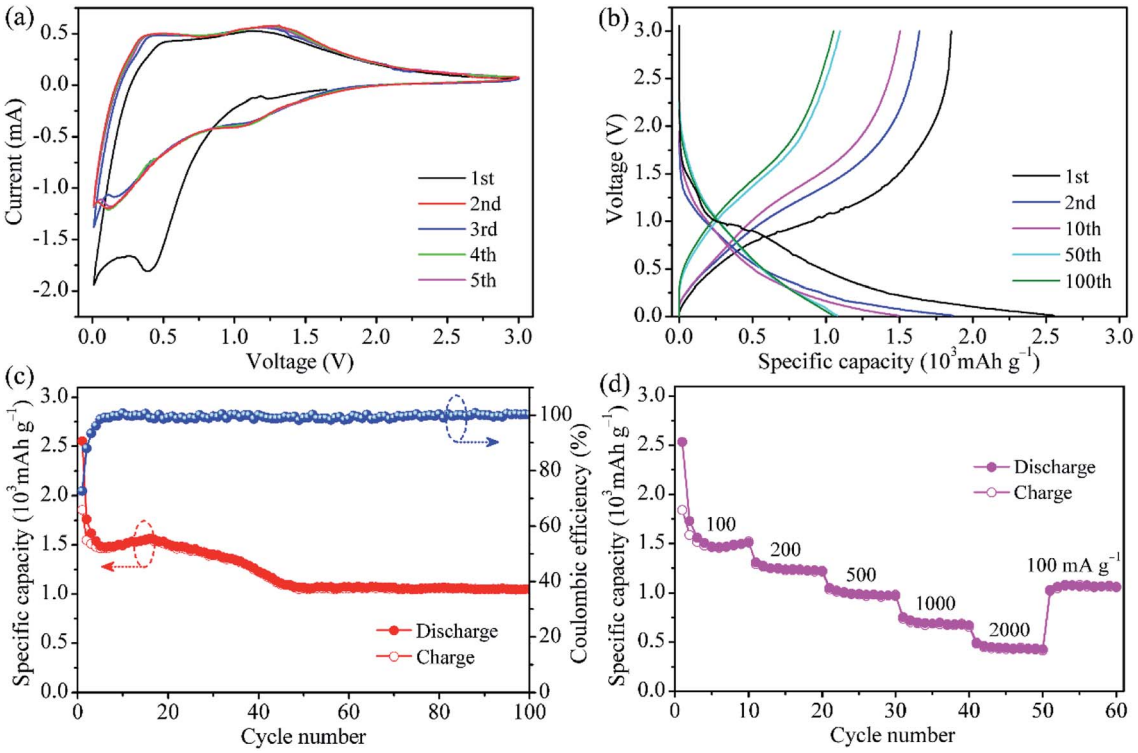

Fig. 3 (a) Cyclic voltammograms, (b) galvanostatic discharge/charge curves for selected cycles at 100 mA g^{-1}, (c) cycling performance and coulombic efficiency at 100 mA g^{-1}, and (d) rate capacities at various current densities for the MoO_2@HPCNFs film electrode.

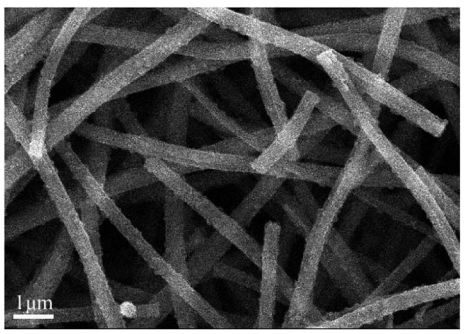

Fig. 4 SEM image of the MoO_2@HPCNFs film electrode after 100 cycles at 100 mA g^{-1}.

prevent the nanoparticle pulverization/aggregation during cycling, which will be conducive to achieving an enhanced and stable electrochemical performance.[26] The HRTEM image (Fig. 2e) reveals that the obtained ultrasmall MoO_2 nanoparticles have a uniform particle size of about 3.5 nm and are homogeneously embedded in the HPCNFs. In addition, the distinct lattice fringes are observed in the HRTEM image, suggesting a comparatively high crystallinity of MoO_2 nanoparticles. The measured interplanar spacings of 0.215, 0.240 and 0.246 nm can be assigned to the (210), (200) and (−202) planes of monoclinic MoO_2, respectively. Moreover, the clear lattice fringes belonging to the graphitic carbon can be observed, which further validates the existence of graphitized carbon in HPCNFs and is well consistent with the Raman results. As shown in Fig. 2f–i, the scanning TEM (STEM) and corresponding elemental mapping images demonstrate the homogeneous distribution O and Mo elements along the HPCNFs, confirming that the MoO_2 nanoparticles with ultrasmall size are evenly dispersed throughout the HPCNFs from another angle. It should be emphasized that such a homogeneous distribution of ultrafine MoO_2 nanoparticles inside the HPCNFs can facilitate the charge transfer and Li^+ ion diffusion kinetics due to the shortened conducting and diffusion paths.[17]

The typical CV curves of MoO_2@HPCNFs film for the initial five cycles are presented in Fig. 3a. In the first cathodic sweep, a broad and large peak at approximately 0.4 V is observed, which is ascribed to the irreversible formation of solid electrolyte interphase (SEI) film on the HPCNFs surfaces.[27] During the subsequent cycles, this peak disappears and one redox couple at about 1.31/1.05 V corresponding to the reversible phase transition of partially lithiated Li_xMoO_2 become relatively distinct.[28,29] At the potential above 1 V, Li^+ is intercalated into MoO_2 to form the solid solution Li_xMoO_2.[23] As the electrode is discharged below 1 V, the as-formed Li_xMoO_2 would reaction with Li^+ and be gradually converted into metallic Mo and Li_2O. From the second cycles onwards, a clear reduction peak appears at around 0.12 V, possibly indicating a more complete conversion reaction from Li_xMoO_2 to Mo and Li_2O.[9] It is worth pointing out that after the first cycle, the CV curves nearly overlap, suggesting the good Li insertion/extraction reversibility of the MoO_2@HPCNFs electrode. In addition, no visible lithiation/delithiation peaks related to the carbon matrix are

Open Access Article. Published on 18 November 2019. Downloaded on 12/9/2025 12:40:41 AM.
This article is licensed under a Creative Commons Attribution-NonCommercial 3.0 Unported Licence.

Table 1 Comparison on electrochemical properties of MoO_2@HPCNFs and some other MoO_2-based anode materials

Sample[ref.]	Current density (mA g^{-1})	Capacity (mA h g^{-1})	Cycle number
MoO_2/CNFs[18]	100	811	100
Carbon coated MoO_2 nanoflowers[31]	90	784.7	60
Hierarchical MoO_2 microspheres[32]	100	709	60
Carbon-coated MoO_2 nanocrystals[33]	200	629	50
Carbon coated MoO_2 nanofibers[34]	50	762.7	100
Hierarchical MoO_2 monolith[35]	200	719.1	20
MoO_2/Mo_2C/C spheres[36]	100	800	100
MoO_2/graphene[37]	60	765.3	40
Mo_2N nanolayer coated MoO_2 hollow nanostructures[38]	100	815	100
Meso-MoO_2/rGO[39]	100	801	50
Present work	100	1055	100

observed below 0.3 V, implying its small contribution to the capacity.

Fig. 3b presents the galvanostatic charge/discharge profiles of MoO_2@HPCNFs at 100 mA g^{-1}. During the first cycle, the MoO_2@HPCNFs electrode delivers large discharge/charge capacities of 2552/1854 mA h g^{-1} with a relatively high initial coulombic efficiency of 72.6%, which indicated that the detrimental reactions between MoO_2 and electrolyte can be significantly alleviated in the MoO_2@HPCNFs. The initial capacity loss is generally attributed to the formation of SEI film and the trapping of Li^+ in the lattices of MoO_2.[9,11] Furthermore, a discharge plateau corresponding to SEI formation is clearly observed and then disappears after the first cycle, which is in good agreement with the CV results. From the 50th cycle, the discharge/charge curves mostly overlap and the capacity remains nearly constant.

Fig. 3c shows the cycling performance of MoO_2@HPCNFs at 100 mA g^{-1}. The slight rise in discharge capacity from 6th to 16th cycle is ascribed to the infiltration of electrolyte and activation of materials. Then, the discharge capacity decreases gradually upon continuous cycling, which may be due to the SEI layer unstability and electrolyte degradation.[30] The capacity finally remains stable with negligible fading after 50 cycles. The anode can deliver a high reversible capacity of 1055 mA h g^{-1} at the 100th cycle, which is obviously higher than the theoretical capacity (838 mA h g^{-1}) of neat MoO_2, demonstrating the efficiently synergistic effect between ultrafine MoO_2 nano-particles and HPCNFs. Furthermore, it needs to be mentioned that the coulombic efficiency reaches approximately 99% after only a few cycles and maintains relatively stable in the subsequent cycles, implying a high electrochemical reversibility and structural stability of MoO_2@HPCNFs.

The rate capability of the MoO_2@HPCNFs electrode is illustrated in Fig. 3d. When the current density is increased, the MoO_2@HPCNFs electrode displays a gradual reduction in the capacity. The specific reversible capacities are about 1510, 1224, 968, 669 and 425 mA h g^{-1} at 100, 200, 500, 1000 and 2000 mA g^{-1}, respectively. More importantly, as the current density is returned to 100 mA g^{-1} even after a high-rate test, the electrode still maintains stable cycling with a reversible capacity of 1060 mA h g^{-1}, indicating the excellent rate performance and strong tolerance for the rapid Li insertion/extraction reaction.

To evaluate the morphological change in the MoO_2@HPCNFs film electrode after 100 charging/discharging cycles at 100 mA g^{-1}, SEM analysis was conducted as shown in Fig. 4. The SEM image clearly reveals that the fibrous morphology of MoO_2@HPCNFs and the formed 3D porous network structure are well-preserved after cycling, which further demonstrates that the as-prepared MoO_2@HPCNFs film electrode has good structural integrity during continuous lithiation and delithiation processes.

Considering the specific capacity and rate capability, the MoO_2@HPCNFs film electrode is clearly superior to the previously reported MoO_2/CNFs prepared without using pore-forming agent and many other MoO_2-based anode materials (Table 1). We believe the enhanced electrochemical performance of MoO_2@HPCNFs should be mainly attribute to the 3D hierarchical structure and synergistic effect. The ultrasmall MoO_2 nanoparticles can be more effectively utilized for Li-storage and can enhance the Li uptake/release kinetics due to the short diffusion pathways. Meanwhile, the abundant meso/macropores in the HPCNFs are able to offer more active sites for Li-storage, and also facilitate the electrolyte penetrate into the inner part of HPCNFs, improving the electrolyte/electrode contacting area. Moreover, the porous 3D conductive network interconnected by HPCNFs is able to provide an efficient and rapid 3D channel for the transportation of both Li ions and electrons, which would increase the electrochemical conductivity and decrease the internal resistance of the MoO_2@HPCNFs electrode. In addition, the combination of hierarchical pores with flexible CNFs matrix may mitigate the pulverization/aggregation of MoO_2 nanoparticles caused by volume change and preserve the structural integrity of the whole film electrode. The combined action of all the above factors leads to the high Li-storage performance of MoO_2@HPCNFs film.

4. Conclusions

In summary, a novel binder-free anode made of flexible self-supporting MoO_2@HPCNFs film has been prepared by the combination of electrospinning with controlled reduction–

 This journal is © The Royal Society of Chemistry 2019

Open Access Article. Published on 18 November 2019. Downloaded on 12/9/2025 12:40:41 AM.
This article is licensed under a Creative Commons Attribution-NonCommercial 3.0 Unported Licence.

carbonization process, in which uniform ultrasmall MoO_2 nanoparticles (~3.5 nm) and plentiful meso/macropores are simultaneously formed and homogenously distributed inside the HPCNFs. Such unique structure endows the composite with a relatively higher reversible capacity and improved rate capability compared to many other MoO_2-based anode materials. The MoO_2@HPCNFs electrode can deliver a high reversible capacity of 1055 mA h g^{-1} after 100 cycles at 100 mA g^{-1}, and it still remains 425 mA h g^{-1} even at a high current rate of 2000 mA g^{-1}. The enhanced electrochemical performance for the MoO_2@HPCNFs film is the end product of the synergistic effect of well-distributed ultrafine MoO_2 nanoparticles and flexible porous 3D conductive network interlinked by HPCNFs, making it a promising anode candidate for LIBs worthy of in-depth study.

Conflicts of interest

There are no conflicts to declare.

Acknowledgements

This work was financially supported by the Natural Science Foundation of Jiangsu Province, China (Grant No. BK20171307) and the Postgraduate Research & Practice Innovation Program of Jiangsu Province (Grant No. SJKY19-2634).

Notes and references

1 T. Kim, W. T. Song, D. Y. Son, L. K. Ono and Y. B. Qi, *J. Mater. Chem. A*, 2019, **7**, 2942.
2 B. Huang, Z. F. Pan, X. Y. Su and L. An, *J. Power Sources*, 2018, **399**, 274.
3 X. Y. Deng, X. F. Chen, Y. Huang, B. B. Xiao and H. Y. Du, *J. Phys. Chem. C*, 2019, **123**, 4721.
4 Y. Yan, F. H. Du, X. P. Shen, Z. Y. Ji, H. Zhou and G. X. Zhu, *Dalton Trans.*, 2014, **43**, 17544.
5 L. M. Zhou, K. Zhang, Z. Hu, Z. L. Tao, L. Q. Mai, Y. M. Kang, S. L. Chou and J. Chen, *Adv. Energy Mater.*, 2018, **8**, 1701415.
6 M. B. Zheng, H. Tang, L. L. Li, Q. Hu, L. Zhang, H. G. Xue and H. Pang, *Adv. Sci.*, 2018, **5**, 1700592.
7 X. C. Pan, S. T. Li, Z. M. Wang, L. Y. Yang, K. J. Zhu, L. Ren, M. Lei and J. Liu, *Mater. Lett.*, 2017, **199**, 139.
8 H. J. Zhang, K. X. Wang, X. Y. Wu, Y. M. Jiang, Y. B. Zhai, C. Wang, X. Wei and J. S. Chen, *Adv. Funct. Mater.*, 2014, **24**, 3399.
9 L. C. Yang, W. Sun, Z. W. Zhong, J. W. Liu, Q. S. Gao, R. Z. Hu and M. Zhu, *J. Power Sources*, 2016, **306**, 78.
10 X. Wang, Y. Xiao, J. Q. Wang, L. N. Sun and M. H. Cao, *J. Power Sources*, 2015, **274**, 142.
11 X. X. Liu, H. H. Xu, Y. H. Huang and X. L. Hu, *Phys. Chem. Chem. Phys.*, 2016, **18**, 19832.
12 Y. L. Chen, Y. Hu, Z. Shen, R. Z. Chen, X. He, X. W. Zhang, Y. Q. Li and K. S. Wu, *J. Power Sources*, 2017, **342**, 467.
13 T. T. Yu, H. L. Liu, M. Huang, J. H. Zhang, D. Q. Su, Z. H. Tang, J. F. Xie, Y. J. Liu, A. H. Yuan and Q. H. Kong, *RSC Adv.*, 2017, **7**, 51807.
14 W. H. Li, M. S. Li, K. R. Adair, X. L. Sun and Y. Yu, *J. Mater. Chem. A*, 2017, **5**, 13882.
15 X. Y. Qian, L. Jin, S. W. Wang, S. S. Yao, D. W. Rao, X. Q. Shen, X. M. Xi and J. Xiang, *RSC Adv.*, 2016, **6**, 94629.
16 L. Zungia, V. Agubra, D. Flores, H. Campos, J. Villareal and M. Alcoutlabi, *J. Alloys Compd.*, 2016, **686**, 733.
17 G. L. Xia, L. J. Zhang, F. Fang, D. L. Sun, Z. P. Guo, H. K. Liu and X. B. Yu, *Adv. Funct. Mater.*, 2016, **26**, 6188.
18 Y. J. Chen, X. T. Yuan, C. Yang, Y. B. Lian, A. A. Razzaq, R. Shah, J. Guo, X. H. Zhao, Y. Peng and Z. Deng, *J. Alloys Compd.*, 2019, **777**, 127.
19 X. Liu, Y. Liu, X. D. Yan, J. L. Lan, Y. H. Yu and X. P. Yang, *Mater. Chem. Front.*, 2019, **9**, 120.
20 J. Xiang, Z. P. Wu, X. K. Zhang and S. S. Yao, *Mater. Res. Bull.*, 2018, **100**, 254.
21 P. Fan, T. S. Mu, S. F. Lou, X. Q. Cheng, Y. Z. Gao, C. Y. Du, P. J. Zuo, Y. L. Ma and G. P. Yin, *Electrochim. Acta*, 2019, **306**, 590.
22 Z. W. Xu, L. Y. Wang, W. Wang, N. Li, C. Chen, C. Y. Li, C. Y. Yang, H. J. Fu and L. Y. Kuang, *Electrochim. Acta*, 2016, **222**, 385.
23 A. Bhaskar, M. Deepa and T. N. Rao, *ACS Appl. Mater. Interfaces*, 2013, **5**, 2555.
24 F. L. Yan, X. Tang, Y. H. Wei, L. B. Chen, G. Z. Cao, M. Zhang and T. H. Wang, *J. Mater. Chem. A*, 2015, **3**, 12672.
25 P. T. Xie, H. Y. Li, B. He, F. Dang, J. Lin, R. H. Fan, C. X. Hou, H. Liu, J. X. Zhang, Y. Ma and Z. H. Guo, *J. Mater. Chem. C*, 2018, **6**, 8812.
26 Q. L. Wei, F. Y. Xiong, S. S. Tan, L. Huang, E. H. Lan, B. Dunn and L. Q. Mai, *Adv. Mater.*, 2017, **29**, 1602300.
27 Y. C. Liu, N. Zhang, C. M. Yu, L. F. Jiao and J. Chen, *Nano Lett.*, 2016, **16**, 3321.
28 Z. Chen, T. Yang, H. M. Shi, T. H. Wang, M. Zhang and G. Z. Cao, *Adv. Mater. Interfaces*, 2017, **4**, 1600816.
29 Y. M. Sun, X. L. Hu, W. Luo and Y. H. Huang, *ACS Nano*, 2011, **5**, 7100.
30 Y. H. Dou, J. T. Xu, B. Y. Ruan, Q. N. Liu, Y. D. Pan, Z. Q. Sun and S. X. Dou, *Adv. Energy Mater.*, 2016, **6**, 1501835.
31 S. S. Tang, L. Y. Yang, J. Liu and D. Fichou, *Mater. Res. Bull.*, 2018, **102**, 277.
32 W. K. Zhai, Y. M. Xu, X. L. Cheng, S. Gao, X. F. Zhang, H. Zhao and L. H. Huo, *Mater. Lett.*, 2015, **145**, 287.
33 L. Zhou, H. B. Wu, Z. Y. Wang and X. W. Lou, *ACS Appl. Mater. Interfaces*, 2011, **3**, 4853.
34 W. Luo, X. L. Hu, Y. M. Sun and Y. H. Huang, *Phys. Chem. Chem. Phys.*, 2011, **13**, 16735.
35 Y. M. Sun, X. L. Hu, J. C. Yu, Q. Li, W. Luo, L. X. Yuan, W. X Zhang and Y. H. Huang, *Energy Environ. Sci.*, 2011, **4**, 2870.
36 M. Ihsan, H. Q. Wang, S. R. Majid, J. P. Yang, S. J. Kennedy, Z. P. Guo and H. K. Liu, *Carbon*, 2016, **96**, 1200.
37 Q. Yang, Q. Liang, J. Liu, S. Q. Liang, S. S. Tang, P. J. Lu and Y. K. Lu, *Mater. Lett.*, 2014, **127**, 32.
38 J. Liu, S. S. Tang, Y. K. Lu, G. M. Cai, S. Q. Liang, W. J. Wang and X. L. Chen, *Energy Environ. Sci.*, 2013, **6**, 2691.
39 S. S. Wang, B. C. Liu, G. L. Zhi, G. R. Xu, Q. Wang and J. Zhang, *Microporous Mesoporous Mater.*, 2017, **246**, 14.